

Recent progress in the microstructurally based creep modelling of Ni-based alloy 617

F. Riedlsperger, T. Wojcik, R. Buzolin, L. Witzmann, G. Zuderstorfer, B. Krenmayr, C. Sommitsch & B. Sonderegger

To cite this article: F. Riedlsperger, T. Wojcik, R. Buzolin, L. Witzmann, G. Zuderstorfer, B. Krenmayr, C. Sommitsch & B. Sonderegger (14 Nov 2023): Recent progress in the microstructurally based creep modelling of Ni-based alloy 617, Materials at High Temperatures, DOI: [10.1080/09603409.2023.2281123](https://doi.org/10.1080/09603409.2023.2281123)

To link to this article: <https://doi.org/10.1080/09603409.2023.2281123>



© 2023 The Author(s). Published by Informa UK Limited, trading as Taylor & Francis Group.



Published online: 14 Nov 2023.



Submit your article to this journal [↗](#)



Article views: 141



View related articles [↗](#)



View Crossmark data [↗](#)

Recent progress in the microstructurally based creep modelling of Ni-based alloy 617

F. Riedlsperger^a, T. Wojcik^b, R. Buzolin^c, L. Witzmann^a, G. Zuderstorfer^a, B. Krenmayr^a, C. Sommitsch^c and B. Sonderegger^a

^aInstitute for Engineering Materials - Metals and Alloys, Johannes Kepler University (JKU) Linz, Linz, Austria; ^bInstitute for Materials Science and Technology, TU Wien, Wien, Austria; ^cInstitute of Materials Science, Joining and Forming (IMAT), Graz University of Technology, Graz, Austria

ABSTRACT

Solid solution strengthened (SSS) Ni-based superalloys, such as A617, show superior creep resistance at 700°C. Established for many years in land- and aero-based gas turbines, these materials are increasingly being considered for use in high-temperature thermal power plants. Apart from SSS, the creep strength in A617 stems from γ' and carbide precipitates. In this work, a microstructurally based creep model for A617 is presented. Mobile dislocations in the model interact with fine grain-interior precipitates, and grain boundaries act as dislocation sources/sinks. The model is capable of simulating creep curves and time-to-rupture (TTR) diagrams based on the evolution of mobile dislocations. At lower stresses, the accuracy of modelled TTR can be improved by adding diffusion creep to dislocation creep. The simulated evolution of dislocation densities is realistic compared to the literature data. The reduction of area of ruptured samples was included in a damage factor, enabling the consideration of creep ductility.

ARTICLE HISTORY

Received 7 March 2023
Accepted 4 November 2023

KEYWORDS

Creep; Ni-based alloy; A617; alloy 617; Inconel 617; modelling; precipitates; dislocation density

Introduction

The efficiency of thermal power plants and aircraft engines increases with higher operating temperatures and pressures, fostering activities in industry and science to develop new creep-resistant materials. Regarding fossil fuels that are burnt in power stations or aeroplanes, raised efficiency goes hand in hand with cost savings and lower CO₂ emissions [1].

One of the material groups predestined for temperatures of 700°C and beyond are SSS Ni-based alloys, combining high creep strength with good formability and excellent oxidation resistance [2]. This work focuses on A617 or Inconel 617 or Ni-22Cr-12Co-9Mo [3] which contains approximately 22 wt.% of Cr, 12 wt.% of Co and 9 wt.% of Mo as well as considerable quantities of Al and Ti [4].

Apart from the SSS mechanism, the outstanding creep performance of A617 can be traced back to the nucleation of small chromium carbides (mostly M₂₃C₆ or M₆C [5]) and of coherent γ' precipitates of type Ni₃(Al,Ti) [2] in the grain-interior. The grain boundaries in A617 are often observed to be decorated by coarse carbides [6] which may under certain circumstances transform into the undesired, brittle, topologically-close packed (TCP) μ -phase [7]. In contrast to other prominent Ni-based alloys (such as Inconel 718 e.g.), the total (volume) phase fraction of precipitates in A617 is observed to remain smaller than 10% [8,9].



During service, an increase in the dislocation density by around one order of magnitude from 10¹³ m⁻² to 10¹⁴ m⁻² has been reported for 700°C and intermediate stresses [5,9]. Possible interaction mechanisms between moving dislocations and grain-interior precipitates are climb, shear, and Orowan looping [10].

In the past, numerous attempts have been made to physically model the creep behaviour of Ni-based alloys by using constitutive rate equations. Significant contributions stem from Dyson [11] for Nimonic 90 or Manonukul et al. [12] for C263, for instance. Both in [11] and [12], gliding dislocations are distinguished from climbing dislocations, and the pinning effect and the dislocation release rate of γ' precipitates are numerically modelled.

In this work, we derive rate-equations for a new A617 creep model based on previous works in martensitic steels by [13–15], considering mobile and static dislocation populations as well as their interaction with grains and with a network of grain-interior (GI) precipitates.

Material and experimental details

Starting point for our simulation are A617 samples from the Austrian contribution to the European Creep Collaborative Committee (ECCC) program with a standard chemical composition according to Table 1.

CONTACT F. Riedlsperger  florian.riedlsperger@jku.at  Institute for Engineering Materials - Metals and Alloys, Johannes Kepler University (JKU) Linz, Linz 4040, Austria

© 2023 The Author(s). Published by Informa UK Limited, trading as Taylor & Francis Group.

This is an Open Access article distributed under the terms of the Creative Commons Attribution License (<http://creativecommons.org/licenses/by/4.0/>), which permits unrestricted use, distribution, and reproduction in any medium, provided the original work is properly cited. The terms on which this article has been published allow the posting of the Accepted Manuscript in a repository by the author(s) or with their consent.

The material was made by vacuum-induction melting and electro-slag re-melting, before being forged into rings with a 220 mm outer diameter, 110 mm inner diameter and 150 mm height.

Solution annealing at 1150°C for 1.5 h served as heat treatment. The ring elements were cut into two halves and re-united by electron-beam welding at company ENPAR. Samples were taken from the block by wire cutting, and four M16 samples without ridges were produced by turning.

Creep tests ran at 700°C with stresses of 165, 170, 175 and 185 MPa. Microstructural analysis was carried out by scanning electron microscopy (SEM) assisted by electron back-scattered diffraction (EBSD), by energy-dispersive X-ray spectroscopy (EDS) and by transmission electron microscopy (TEM). An overview of used microscope types, modes, equipment and acceleration voltages, U_a , is given in Table 2.

The as-received condition and the 700°C/165 MPa ruptured creep sample were investigated after a test duration of 34,220 h. In this work, only insights into the microstructure of the crept specimen are provided. Further details on experimental results (including more qualitative and quantitative details) can be found in [16].

Simulation details

A stepped thermodynamic equilibrium of A617 was calculated by MatCalc version 6.03, using the free Ni-database 'mc_ni_v2.034.tdb'. Creep simulations were carried out in MatLab version 2021b.

Creep model

In this work, we adapt a recently published mean-field dislocation creep model for Cr-steels [15] to the microstructural features observed in A617. We remove low-angle boundaries (subgrains) from the model, and only consider mobile - as well as static dislocations, with densities ρ_m and ρ_s , respectively. As

a source of dislocation emission and potential absorption barrier, we introduce high-angle grain boundaries (HAGB) with a radius R_{gb} . Furthermore, we implement the effect of dislocation pinning and release [11,12] by a network of grain-interior γ' and $M_{23}C_6$ particles, using an interparticle spacing λ [17]. The following production, annihilation and interaction mechanisms are reflected in the rate equations, and are visualised in Figure 1:

- (a) Frank-Read sources in the grain-interior
- (b) Dislocation emission from high-angle grain boundaries
- (c) Long dislocation segment release from particles by climbing
- (d) Short dislocation segment release from particles (proportional to their phase fraction) by climbing [11]
- (e) Short dislocation segment release from particles by gliding [12]
- (f) Dislocation absorption at grain boundaries
- (g) Dislocation pinning at grain-interior particles (γ' and $M_{23}C_6$) [11]
- (h) Retarding effect at dislocation networks
- (i) Static recovery; annihilation by climbing [13]
- (j) Dynamic recovery; (strain-rate proportional) annihilation by gliding [13]

A mathematical formulation of terms (a) to (j) is provided in eq. (2) and in eq. (3) of Table 3, describing the evolution of ρ_m and ρ_s over service time, respectively. The interparticle distance, λ , can be calculated from precipitate number density N_v and the mean radius r_p [17], see eq. (4). For the case of precipitates being not present (or having not yet nucleated at the beginning of service), a mean obstacle distance of a dislocation network, \bar{h}_1 , has been introduced, see eq. (5), following an idea from [12]. v_g stands for the glide velocity, as given in eq. (6), and v_c for the climb velocity, see eq. (7) [15]. Both v_g and v_c require an internal stress σ_i for which a Taylor law was applied, see eq. (8) [20].

Table 1. Chemical composition of A617 in wt.% (adopted from [4]).

Ni	Cr	Co	Mo	Fe	Al	Ti	Cu	Mn	Si	C	P	S	B
bal	20–23	11–14	8.5–10	<2	0.7–1.4	0.2–0.6	<0.5	<0.2	<0.2	0.05–0.1	<0.01	<0.01	<0.006

Table 2. Microscope types and experimental techniques used for A617 investigation (see also [16]).

Microscope	Type	Mode	U_a
TEM	FEI Tecnai F20	Bright-/Dark-field	200 kV
SEM	Tescan Mira3	Secondary electron (SE) Backscattered electron (BSE)	10 to 25 kV
SEM-EBSD	Hikari EBSD Camera	Electron backscattered diffraction (EBSD)	30 kV

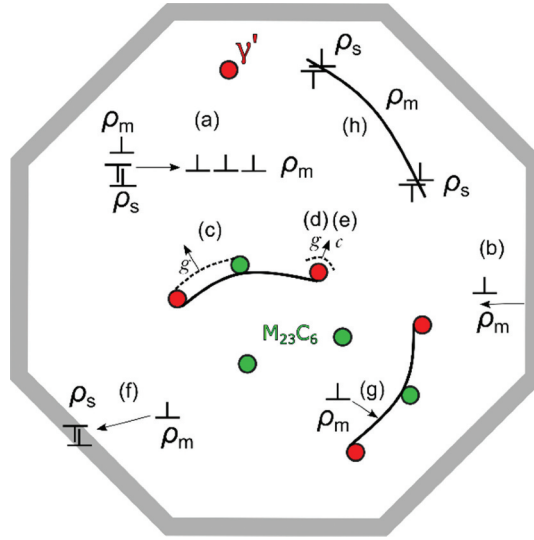


Figure 1. Microstructural interactions (a)-(j) inside a HAGB (with radius R_{gb}) in the new A617 model.

Table 3. Equations and terms in the new A617 creep model and their source.

Description of equations and terms	Eq.	Ref.
Creep strain rate (dislocation creep):		[14]
$\frac{d\epsilon_{disl}}{dt} = \frac{b \cdot \rho_m \cdot v_g}{M \cdot (1 - D_{cav})}$	(1)	[15,18] [19]
The evolution rate of mobile dislocation density:		
$\frac{d\rho_m}{dt} = \underbrace{\rho_m(\sqrt{\rho_m} + \sqrt{\rho_s})u_g}_{(a)} + \underbrace{\frac{\beta\rho_s R_{gb}}{\tilde{h}_1^2} v_g}_{(b)} + \underbrace{\frac{\rho_s}{\lambda} v_c}_{(c)} + \underbrace{\frac{\rho_s f_v b}{r_p} v_c}_{(d)} + \underbrace{\frac{\rho_s}{2r_p} v_g}_{(e)} - \underbrace{\frac{\rho_m}{2R_{gb}} u_g}_{(f)}$ $- \underbrace{\frac{\rho_m}{\lambda} u_g}_{(g)} - \underbrace{\frac{\rho_m}{\tilde{h}_1} u_g}_{(h)} - \underbrace{8\rho_m^{3/2} U}_{(i)} - \underbrace{\delta_{anh}(\rho_m + \rho_s)\rho_m u_g}_{(j)}$	(2)	new
The evolution rate of static dislocation density:		
$\frac{d\rho_s}{dt} = \underbrace{\frac{\rho_m}{2R_{gb}} u_g}_{(f)} + \underbrace{\frac{\rho_m}{\lambda} u_g}_{(g)} + \underbrace{\frac{\rho_m}{\tilde{h}_1} u_g}_{(h)} - \underbrace{\frac{\rho_s f_v b}{r_p} v_c}_{(b)} - \underbrace{\frac{\rho_s}{\lambda} v_c}_{(c)} - \underbrace{\frac{\rho_s}{2r_p} v_g}_{(e)} - \underbrace{\frac{8U_c}{\tilde{h}_1}}_{(i)} - \underbrace{\delta_{anh} \cdot \rho_s \cdot \rho_m \cdot u_g}_{(j)}$	(3)	new
Interparticle spacing of grain-interior precipitates (index "i" for $M_{23}C_6$ and γ):		
$\lambda = \sqrt{\frac{\ln(3)}{2\pi \sum_i (N_{v,i} r_{p,i})} + (2r_A)^2} - 2r_A$ $r_A = \sqrt{\frac{2}{3} \cdot \frac{\sum_i (N_{v,i} r_{p,i}^2)}{\sum_i (N_{v,i} r_{p,i})}}$	(4)	[17]
Mean obstacle spacing of a dislocation network:		
$\tilde{h}_1 = \frac{0.8}{\sqrt{\rho_m + \rho_s}}$	(5)	new
Glide velocity of dislocations		
$u_g = a_1 \cdot \exp\left\{-\frac{Q}{k_B T}\right\} \cdot \exp\left\{-\frac{\sigma_i \cdot V_d}{k_B T}\right\} \cdot 2 \cdot \sinh\left\{\frac{\sigma_{app} \cdot V_d}{k_B T}\right\}$	(6)	[15]
Climb velocity of dislocations:		
$u_c = \left\{ \frac{2 \cdot \pi \cdot \eta_v \cdot D_s}{[1 - \eta_v \cdot \ln(L_v / \sqrt{\rho_i})] \cdot b} + \frac{2 \cdot \pi \cdot b \cdot D_{pp}}{L_p^2} \right\} \cdot \exp\left\{-\frac{\sigma_i \cdot \Omega}{k_B T}\right\} \cdot 2 \cdot \sinh\left\{\frac{\sigma_{app} \cdot \Omega}{k_B T}\right\}$	(7)	[15]
Internal stress:		
$\sigma_i = a M G b \cdot \sqrt{\rho_m + c_s \rho_s}$	(8)	[20]
Cavitation damage rate:		
$\dot{D}_{cav} = \underbrace{A}_{1/Z} \cdot \dot{\epsilon}$	(9)	[21]
Creep strain rate (Coble creep/diffusion creep)		
$\frac{d\epsilon_{coble}}{dt} = A_c \frac{D_{gb} \delta_{gb} \sigma_{app} \Omega}{(2R_{gb})^3 k_B T}$	(10)	[22]

After solving the differential equation system, the **strain rate from dislocation creep**, $\dot{\epsilon}_{disl}$, is determined from a modified Orowan's law, by multiplying mobile dislocation density ρ_m with the glide velocity v_g and the Burgers vector b , see eq. (1) [14,15,18,19].

The cavitation damage factor, D_{cav} (and its evolution over time), was adopted from [21], see eq. (9). The precipitate damage factor (as previously used in [15] and [16] based on a concept of [20]) was removed from the modified Orowan's law in this work. The

strain rate share from diffusion creep, $\dot{\epsilon}_{coble}$, is calculated from a Coble creep law according to [22], taking into account the effect of grain boundary diffusion (with a coefficient D_{gb}), see eq. (10).

Model setup and input parameters

The chosen input parameters for our A617 dislocation creep model can be seen in Table 4. Most parameters come from literature or from the experimental evaluation of the precipitate and dislocation state in the as-received state and in the 700°C/165MPa crept condition [16]. Important microstructural start values comprise the mobile (ρ_m) and static dislocation density (ρ_s) as well as the grain radius (R_{gb}); please see the end of Table 4. A few parameters had to be optimised, see Table 5. It includes the pre-factor of the glide velocity a_1 , the activation volume V_r (literature data suggest some potential range, see Table 4), the dislocation interaction factor α and the pipe diffusion coefficient D_{vp} . The parameters required for assessing the diffusion creep share are provided in Table 6, including the pre-factor of the Coble creep law, A_c , the grain boundary diffusion coefficient D_{gb} and the grain boundary width, δ_{gb} .

Experimental results

The as-received state of A617 after normalising was almost free of precipitates (except for a low number of large, primary, Ti-rich MX particles) [16]. By contrast,

in the 700°C/165MPa crept condition after 34,220 h, coherent γ' precipitates with a size of 108 ± 45 nm, and $M_{23}C_6$ carbides with a diameter of 50 ± 20 nm were identified by TEM-EDX in the grain-interior [16], see Figure 2a. The number density of γ' was evaluated with method 3 from [37], yielding $8.9 \cdot 10^{19} \text{ m}^{-3}$ [16]. The number density of $M_{23}C_6$ in the grain-interior was roughly estimated to be 10^{20} m^{-3} [16]. If these number densities are combined with the stated diameters, phase fractions of around 5.8% for γ' and of approximately 1% for $M_{23}C_6$ can be calculated.

Dislocations were observed to either surmount γ' particles by climbing or by forming Orowan loops around them, see Figure 2b. Dislocation density was found by TEM to rise from around $4 \cdot 10^{13} \text{ m}^{-2}$ in the as-received state (not shown here) to approximately $2 \cdot 10^{14} \text{ m}^{-2}$ after 34,220 h at 700°C/165 MPa, see Figure 2b [16].

High-angle grain boundaries act as strong sources of dislocation emission, as demonstrated in a map of geometrically necessary dislocations (GNDs) from SEM-EBSD of the 700°C/165MPa crept condition after 34,220 h [16], see Figure 3.

The grain boundaries themselves were surrounded by a sequence of large $M_{23}C_6$ particles and of TCP μ -phase in the range of 1–2 μm , see Figure 4 from SEM, including an EDX mapping of Cr and Mo [16]. In [16], we re-identified and confirmed the presence of μ -phase by selected area diffraction (SAD) in TEM, by MatCalc equilibrium simulations (see also in the next section),

Table 4. Input parameters for A617 dislocation creep model with sources (table modified from [16], where a detailed description of all parameters is provided).

Input	Value	Material (Group)	Source
Parameters from Literature			
a_g	$3.59 \cdot 10^{-10} \text{ m}$	Ni- fcc	[23]
β	0.0375	Model specific value	[15]
b	$2.54 \cdot 10^{-10} \text{ m}$	Ni- fcc	[23]
c_s	0.3		[16,20]
δ_{anh}	$6 \cdot 10^{-9} \text{ m}$	Ni- fcc (750K)	[24]
D_s	$9.0 \cdot 10^{-20} \text{ m}^2/\text{s}$	Ni- fcc (bulk diffusion 700°C)	[25]
E_{pipe}	$4.03\text{--}5.52 \cdot 10^{-19} \text{ J}$	A617 (700°C)	[26–28]
η_v	10^{-5}	η_v calculated for a stacking fault energy of 0.1 J/m ² in A617 [23]	[13]
G	64 GPa	A617 (700°C)	[29]
k_B	$1.38065 \cdot 10^{-23} \text{ J/K}$	Fundamental constant	[30]
M	3	Crystals (approximation)	[20]
Q	$5 \cdot 10^{-19}$ to $7 \cdot 10^{-19} \text{ J}$	C263	[12]
	$6 \cdot 10^{-20}$ to $2 \cdot 10^{-19} \text{ J}$	Ni- fcc	[31]
V_r	$250 \cdot b^3$	Coarse-grained Ni	[32]
	$100 \cdot b^3$	Ni with a grain size of 500 μm	[33]
ν	0.3	A617	[29]
Microstructural Input Parameters (Start Values)			
Input	Value	Material (Group)	Source
$\rho_{m,0}$	$4 \cdot 10^{13} \text{ m}^{-2}$	A617 as-received condition	TEM [16]
$\rho_{s,0}$	$4 \cdot 10^{12} \text{ m}^{-2}$	A617 as-received condition	10% of $\rho_{m,0}$ [20]
R_{gb}	250 μm	A617 as-received condition	EBSD [16]

Table 5. Optimized input parameters for the A617 dislocation creep model (table modified from [16]).

Parameter	Value	Unit	Parameter	Value	Unit
a_1	$6 \cdot 10^{-13}$	m/s	a	0.03	-
V_r	$145 \cdot \Omega = 103 \cdot b^3$	m^3	D_{vp}	$1.4 \cdot 10^{-19}$	m^2/s

Table 6. Parameters for calculation of the A617 diffusion creep share.

Parameter	Value	Unit	Source
A_c	48	-	[22,34]
D_{gb}	$3.4 \cdot 10^{-12}$	m^2/s	[35]
δ_{gb}	$5 \cdot b$	m	[36]

and by finding characteristic stacking faults [38] visible inside the particles in TEM.

Results of thermodynamic precipitate simulation

Thermodynamic MatCalc simulations identified all equilibrium phases in our batch of A617 and estimated their phase fraction. Figure 5 shows the result of a stepped equilibrium calculation between 400 and 1600°C. At the relevant temperature of 700°C, around 5.2 mol.% of γ' and 1.3 mol.% of $M_{23}C_6$ is predicted, see Figure 5. This agrees well with the experimentally found phase fractions of 5.8 mol.% γ' and around 1 mol.% for $M_{23}C_6$. The theoretically simulated equilibrium phase fraction of 3.8 mol.% for μ -phase has to be critically questioned, since μ -phase formation is believed to be a transient process, either transforming from $M_{23}C_6$ and/or nucleating adjacent to $M_{23}C_6$ located at the grain boundaries [7]. A slow transformation might occur, similar to the proposed transition of MX carbides into the Z-phase in Cr-steels [39].

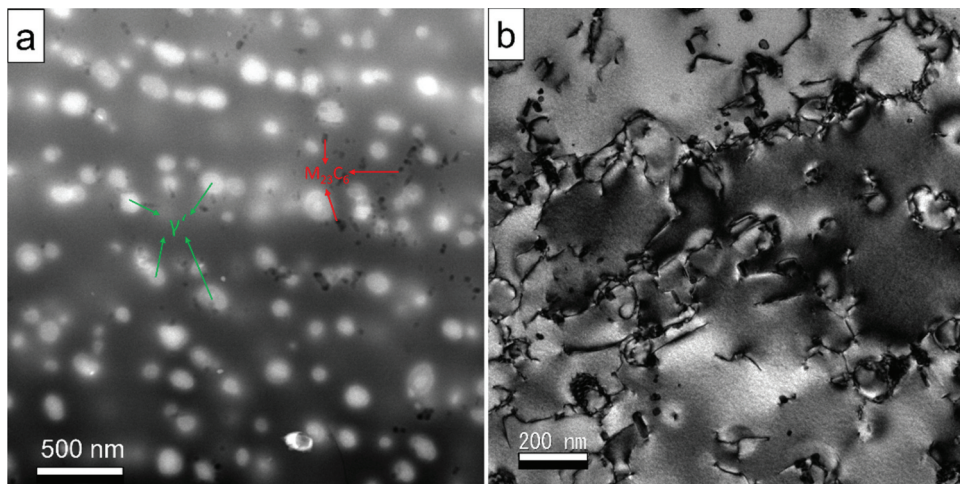


Figure 2. Microstructure of 700°C/165MPa crept condition after 34220h of creep (gauge section); a) γ' and $M_{23}C_6$ precipitates; b) dislocation interaction with γ' (climb and Orowan mechanism).

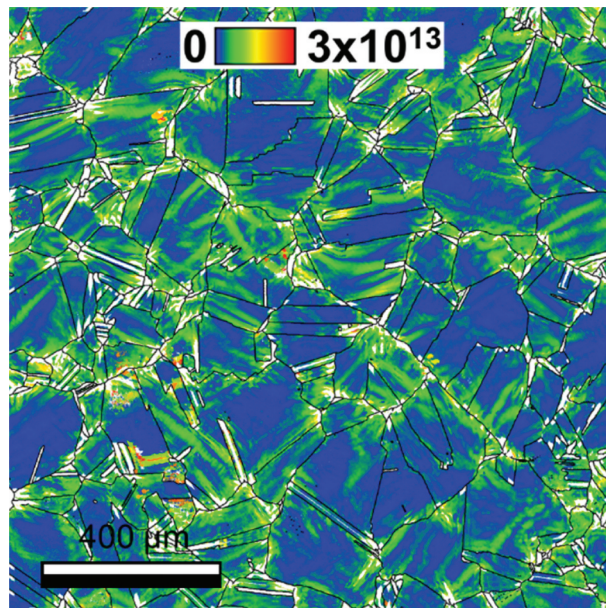


Figure 3. GND map from EBSD data of the 700°C/165MPa crept condition after 34220h of creep (gauge section); modified from [16].

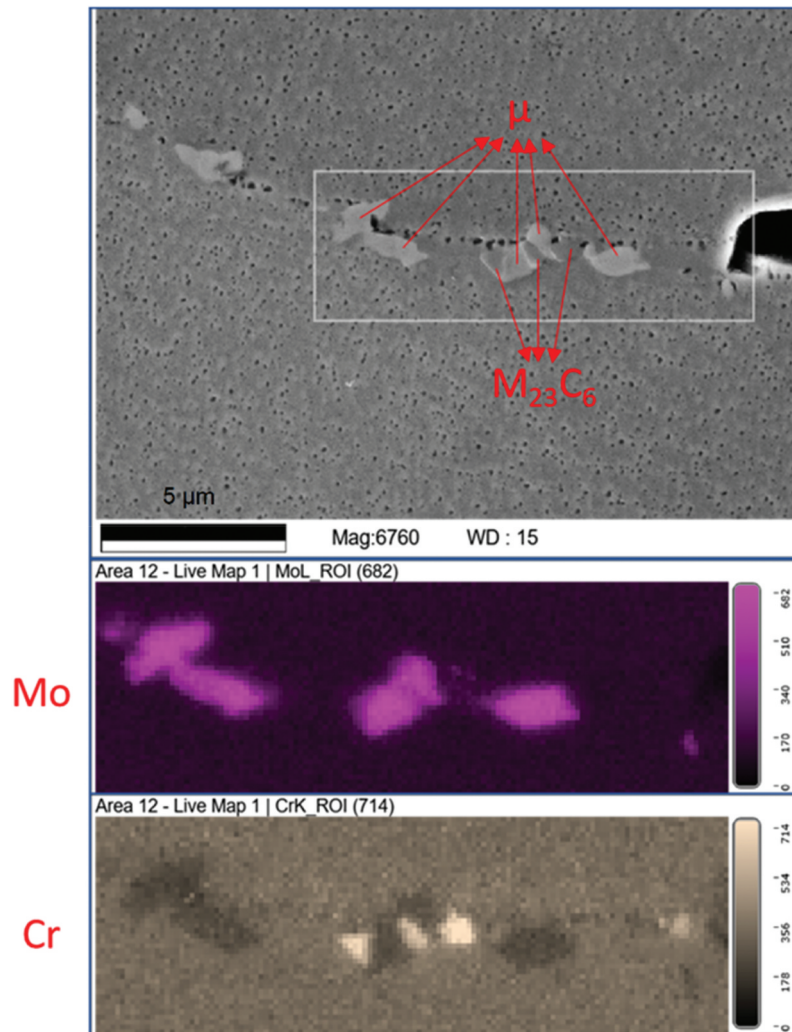


Figure 4. Sequences of $M_{23}C_6$ and of μ -phase decorating the grain boundaries of A617 after 34220h of creep at 700°C/165MPa visible in SEM; with a mo- and Cr-mapping below (modified from [16], where also further proof for existence of μ -phase is provided).

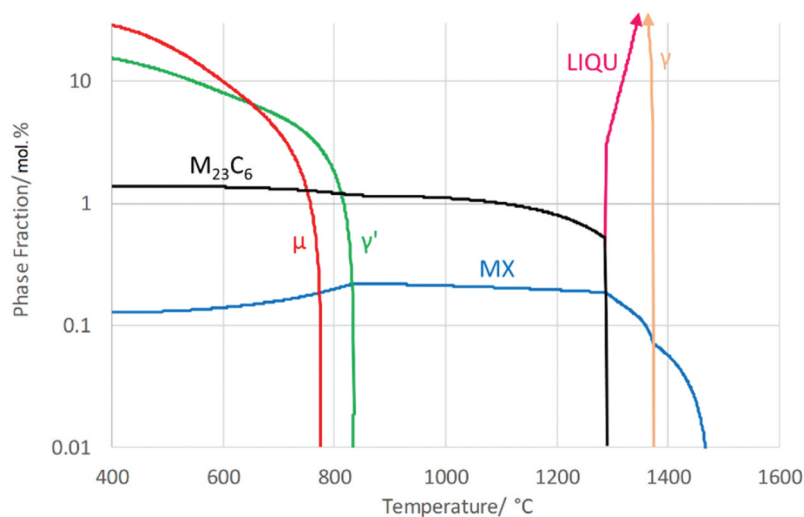


Figure 5. Stepped equilibrium calculation of A617 in MatCalc 6.03 for phase fractions in a temperature range of 400 to 1600°C.

Results of precipitate evolution fit

The precipitate radius evolution of γ' and grain-interior (GI) $M_{23}C_6$ ($r_{p,i}$) between the start of service and the measured sizes after 34,420 h of creep was fitted by

a cubic Ostwald ripening law [40], see Figure 6a. An Avrami-type equation [41] served to model the nucleation and growth stage for the rise of precipitate phase fractions ($f_{v,i}$), until reaching the coarsening

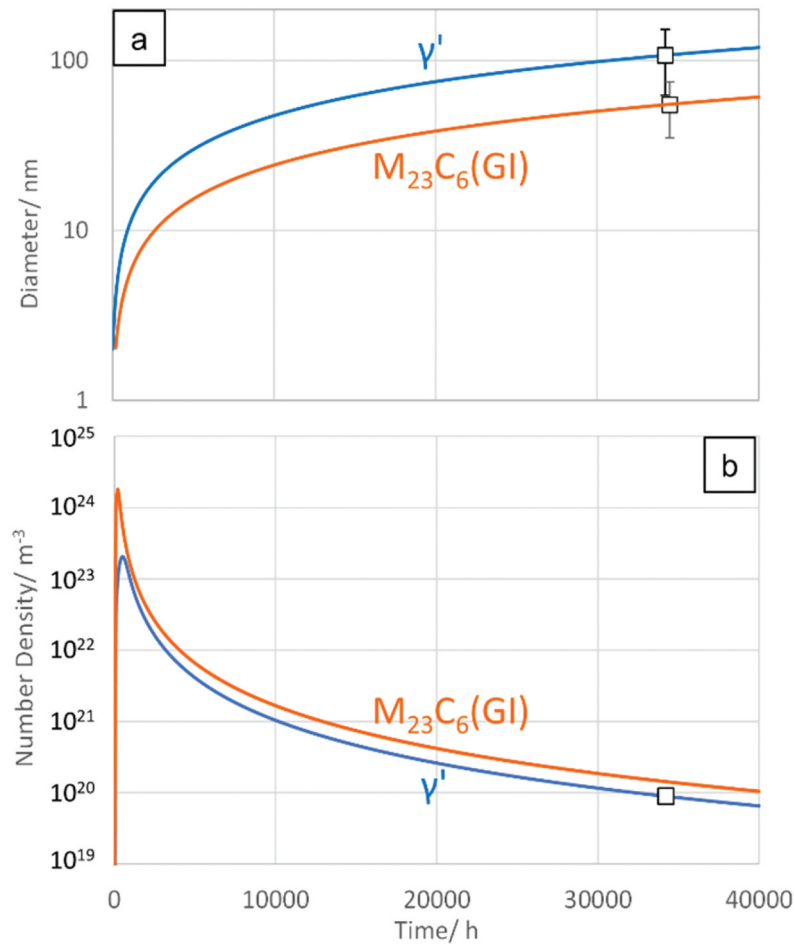


Figure 6. Fitted evolution of a) the radius $r_{p,i}$ of γ' and of grain-interior (GI) $M_{23}C_6$ and of b) the number density $N_{v,i}$ of γ' and of $M_{23}C_6(GI)$; both for service at 700°C; figure mod. From [16].

stage, i.e. the constant level of equilibrium phase fractions indicated before. The number density evolution of γ' and grain-interior (GI) $M_{23}C_6$ ($N_{v,i}$) was then calculated from $f_{V,i}$ divided by the precipitate volume (spheres with a radius $r_{p,i}$), see Figure 6b. The evolution of the total interparticle distance λ was evaluated by eq. (4). It is not explicitly shown here, but can be found in [16]. Please note that the modelling of grain-boundary (GB) precipitate evolution, i.e. of $M_{23}C_6$ and of μ -phase, is not directly addressed in this work. However, we have proposed a simple concept of considering GB particles within a precipitate damage concept in a modified Orowan's law elsewhere [16].

Results of creep simulation

After setting up the A617 creep model and fitting the GI precipitate data of γ' as well as $M_{23}C_6$, creep curves at 700°C and for applied stresses between 165 and 215 MPa were calculated. One time, the strain rate was calculated only by the modified Orowan's law for

dislocation creep (eq. 1; simulation 1), and secondly as a comparison- diffusion creep was added (eq. 10), i.e. the strain rate contributions from dislocation creep and diffusion creep were summed up (simulation 2). Selected creep curves for 170 MPa, 185 MPa and 200 MPa from simulation 1 (dislocation creep) and simulation 2 (combined dislocation- and diffusion creep) are plotted in Figure 7. The lower the applied stress was chosen, the more pronounced was the difference in creep life, when considering diffusion creep (additional to dislocation creep) compared to excluding it.

After reaching 100% of cavitation damage, see eq. (9), all simulations ended at a strain, respectively, an elongation of 4% which is believed to be close to the reality of the four samples (although exact values were not measured). Possible reasons for the low ductility of the tested A617 material are the electron beam welding procedure and the occurrence of TCP μ -phase at grain boundaries.

Figure 8 demonstrates the predicted rupture times for the two A617 simulations at 700°C between 165 and 215 MPa. The virtual TTR diagram was constructed from the rupture times of all modelled creep curves in the corresponding stress range. It turns out

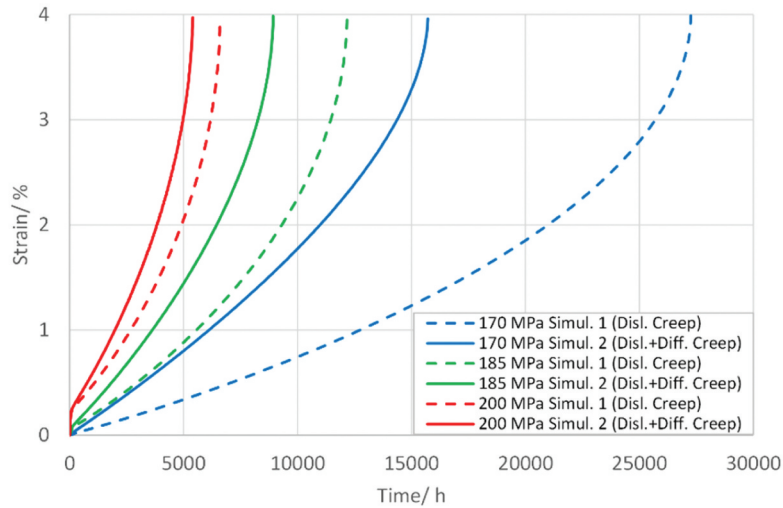


Figure 7. Modelled creep curves of A617 for simulation 1 (dislocation creep) and simulation 2 (dislocation + diffusion creep) at 700°C and 170, 185 and 200 MPa.

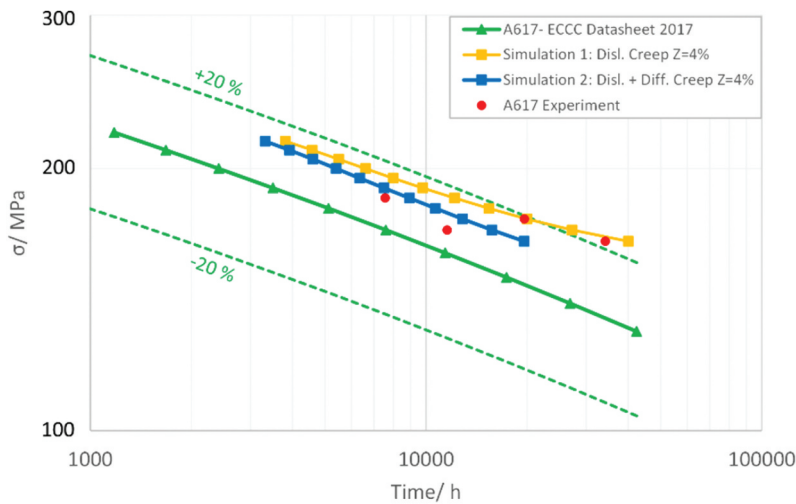


Figure 8. Modelled TTR diagram for A617 at 700°C for simulation 1 (dislocation creep) and for simulation 2 (dislocation + diffusion creep); with a comparison to experimental data points in red and to A617 reference data from ECCC [42]; figure mod. From [16].

that the slope of simulation 2 shows a better agreement with ECCC reference data [42] than simulation 1. Simulation 2 also seems well positioned between the experimental points of A617 from the Austrian ECCC programme, slightly underestimating TTR at 165 and 175 MPa, overestimating TTR for 170 and 185 MPa, but overall representing a good compromise. The large scatter of the four experimental points is believed to be a consequence of the electron beam welding process.

The reduction of area (Z) after failure was measured to lie between 3% and 7% for the tested A617 samples, see the black arrows connected to the experimental red points in Figure 9. Between the pre-factor of the cavitation damage law (A) and the reduction of area (Z), we propose an inversely proportional relation, see eq. (9). This implies that $Z = 8\%$ e.g. corresponds to $A = 12.5$,

whereas $Z = 2\%$ would result in $A = 50$. Subsequently, it is possible to vary virtually the ductility level of samples in the simulation, as shown in Figure 9. By that means, agreement between our four experimental data points and the creep simulation (simulation 2 in this case) can be significantly improved.

A strategy to verify the microstructural correctness of our creep model is to track the evolution of mobile dislocation density (ρ_m) and to compare modelled values (after rupture) to literature data on A617. Figure 10 shows the modelled, time-dependent evolution of ρ_m for 165, 175 and 200 MPa at 700°C. ρ_m in the frame of creep seems to increase one to two orders of magnitude, starting from $5 \cdot 10^{13} \text{ m}^{-2}$ and reaching a plateau (obviously a kind of equilibrium density) of 10^{14} to 10^{15} m^{-2} . The higher the applied stress, the

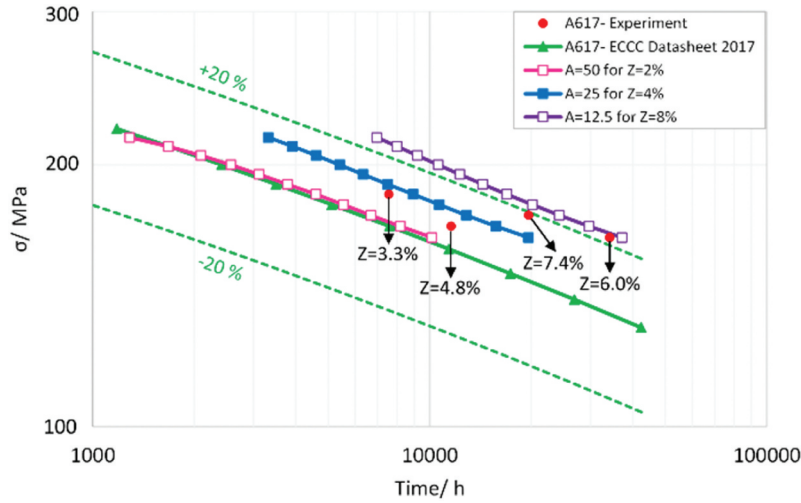


Figure 9. Variation of ductility for simulation 2 (disl.+ diff. creep): test of cases $Z=2\%$ (more brittle) and $Z=8\%$ (more ductile) compared to the reference case $Z=4\%$ shown before; measured Z values are provided below black arrows connected to experimental data points in red; figure mod. From [16].

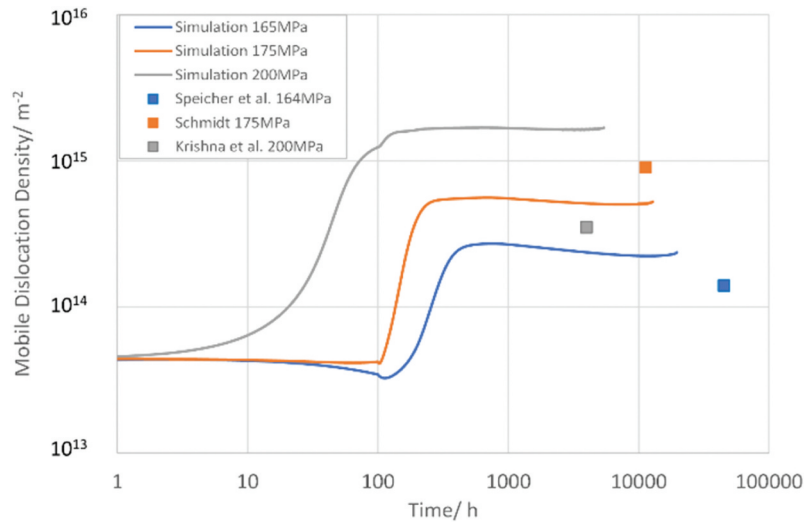


Figure 10. Evolution of mobile dislocation density in simulation at 165, 175 and 200 MPa vs. data points from Speicher et al. [5] (164 MPa), Schmidt [43] (175 MPa) and Krishna et al. [9] (200 MPa); figure mod. From [16].

higher is the increase and the more mobile dislocations are emitted according to our simulation. A similar level of ρ_m after failure is reported in the literature [5,9,43], from where respective data points were included in the diagram. However, the trend in literature is not entirely consistent, i.e. ρ_m after creep rupture at 200 MPa [9] is below ρ_m after creep rupture at 175 MPa [43]. This may be related to the fact that dislocation densities (especially with TEM) are challenging to quantify, the scatter is often large, inhomogeneities may occur and the result also depends strongly on the measurement method [44].

Conclusion and outlook

This work presented recent progress in the physically-based creep modelling of Ni-based alloy 617. Various interactions between dislocations and precipitates (γ'

and $M_{23}C_6$) were considered within a mean-field rate equation approach capable of calculating creep curves and TTR diagrams based on the evolution of mobile dislocation density. Microstructural input data as start values were adopted from measurements (TEM and EBSD) and from literature. Equilibrium phase fractions of precipitates were simulated by MatCalc, enabling- together with TEM size data- a fitting procedure for the evolution of the particle radius, number density and interparticle distance over time. Both simulated TTR and the predicted level of dislocation density after rupture fit well to available reference data on A617. Furthermore, an inversely proportional relationship between the reduction of area (Z) and the cavitation damage factor (D_{cav}) was found, making it possible to vary ductility in the model. By this means, the accuracy of our simulation compared to four experimental TTR points with differing Z values was

significantly improved. A remaining open point is the treatment of grain boundary precipitates and their correct implementation into either the rate equations or the damage concept. It first requires a better understanding of how and when μ -phase nucleates or transforms from $M_{23}C_6$. Another critical issue is the evaluation of potential grain growth - which due to a lack of experimental data was not possible, making us assume the grain size to remain constant in the current approach. Application of the new A617 model to different temperatures is planned, to create a multi-stress/multi-temperature framework on a physical basis, such as demonstrated for martensitic Cr-steel P92 in [45]. We also aim at implementing the model into the software CreeSo [46].

Acknowledgments

F.R., G.Z. and B.S. gratefully acknowledge the support of the Austrian Science Fund FWF in the frame of the project “Software Development on Dislocation Creep in Alloys” (P-31374). F.R. thanks the European Creep Collaborative Committee (ECCC) for fruitful discussions, in particular Magdalena Speicher, Eleonora Poggio, Andrea Riva, Mike Spindler, Chris Bullough and David Allen. F.R. and L.W. are indebted to Nasr Ghoniem for e-mail debates about the structure of rate equation terms in his famous 1990 model. R.B. fosters the Christian Doppler Laboratory for Design of High-Performance Alloys by Thermomechanical Processing with the support of the Christian Doppler Society. T.W. wishes to thank USTEM at TU Wien for access to TEM. All authors thank Jörg Steiner from Voestalpine Foundry Linz for permission to publish the presented A617 rupture data from the Austrian ECCC program.

Disclosure statement

No potential conflict of interest was reported by the author(s).

Funding

The work was supported by the Austrian Science Fund [P-31374].

ORCID

F. Riedlsperger  <http://orcid.org/0000-0002-0310-1937>

References

- [1] Hald J. Microstructure and long-term creep properties of 9–12% Cr steels. *Int J Pres Ves Pip.* 2008;85(1–2):30–37. doi: [10.1016/j.ijpvp.2007.06.010](https://doi.org/10.1016/j.ijpvp.2007.06.010)
- [2] Klöwer J. Alloy 617 and derivatives. In: Di Gianfrancesco A, editor. *Materials for ultra-supercritical and advanced ultra-supercritical power plants*, Elsevier; 2017. pp. 547–570. [10.1016/B978-0-08-100552-1.00016-6](https://doi.org/10.1016/B978-0-08-100552-1.00016-6)
- [3] Gariboldi E, Cabibbo M, Spigarelli S, et al. Investigation on precipitation phenomena of Ni–22Cr–12Co–9Mo alloy aged and crept at high temperature. *Int J Pres Ves Pip.* 2008;85(1–2):63–71. <https://www.doi.org/10.1016/j.ijpvp.2007.06.014>
- [4] Riva A, Spindler M, Krein R, et al., “The new ECCC datasheet for alloy 617: multi-regime models to cover a wide range of temperature,” *Proc. 5th Int. ECCC Creep & Fracture Conf.*, October 2021, Online, pp. 267–280.
- [5] Speicher M, Kauffmann F, Shim J-H, et al. Microstructure evolution in alloy 617 B after a long-term creep and thermal. *Mater Sci Eng.* 2018; A711:165–174. doi: [10.1016/j.msea.2017.11.004](https://doi.org/10.1016/j.msea.2017.11.004)
- [6] Martino SD, Faulkner R, Hogg S, et al. Characterisation of microstructure and creep properties of alloy 617 for high-temperature applications. *Mater Sci Eng.* 2014;619:77–86. doi: [10.1016/j.msea.2014.09.046](https://doi.org/10.1016/j.msea.2014.09.046)
- [7] Jiang H, Dong J, Zhang M. Phase transformation of alloy 617B during 10000h aging: an element redistribution-related process. *J Alloys Compd.* 2018;765:586–594. doi: [10.1016/j.jallcom.2018.06.229](https://doi.org/10.1016/j.jallcom.2018.06.229)
- [8] Yamasaki S, Mitsuhara M, Nakashima H. Deformation Microstructure and fracture behavior in creep-exposed alloy 617. *Mater Trans.* 2017;58(3):442–449. doi: [10.2320/matertrans.M2016407](https://doi.org/10.2320/matertrans.M2016407)
- [9] Krishna R, Atkinson H, Hainsworth S, et al. Gamma prime precipitation, dislocation densities, and TiN in creep-exposed Inconel 617 alloy. *Metall Mater Trans A.* 2016;47(1):178–193.
- [10] Benz J, Carroll L, Wright J, et al. Threshold stress creep behavior of alloy 617 at intermediate temperatures. *Metall Mater Trans A.* 2014;45(7):3010–3022. doi: [10.1007/s11661-014-2244-y](https://doi.org/10.1007/s11661-014-2244-y)
- [11] Dyson B. Microstructure based creep constitutive model for precipitation strengthened alloys: theory and application. *Mater Sci Technol.* 2009;25(2):213–220. doi: [10.1179/174328408X369348](https://doi.org/10.1179/174328408X369348)
- [12] Manonukul A, Dunne F, Knowles D. Physically-based model for creep in nickel-base superalloy C263 both above and below the gamma solvus. *Acta Mater.* 2002;50(11):2917–2931. doi: [10.1016/S1359-6454\(02\)00119-2](https://doi.org/10.1016/S1359-6454(02)00119-2)
- [13] Ghoniem N, Matthews J, Amodeo R. A dislocation model for creep in Engineering Materials. *Res Mech.* 1990;29:197–219.
- [14] Yadav S, Sonderegger B, Stracey M, et al. Modelling the creep behaviour of tempered martensitic steel based on a hybrid approach. *Mater Sci Eng.* 2016; A662:330–341. doi: [10.1016/j.msea.2016.03.071](https://doi.org/10.1016/j.msea.2016.03.071)
- [15] Riedlsperger F, Krenmayr B, Zuderstorfer G, et al. Application of an advanced mean-field dislocation creep model to P91 for calculation of creep curves. *Materialia.* 2020;12:100760. doi: [10.1016/j.mta.2020.100760](https://doi.org/10.1016/j.mta.2020.100760)
- [16] Riedlsperger F, Wojcik T, Buzolin R, et al. Microstructural insights into creep of Ni-based alloy 617 at 700°C provided by electron microscopy and modelling. *Mater Charact.* 2023;198:112720. doi: [10.1016/j.matchar.2023.112720](https://doi.org/10.1016/j.matchar.2023.112720)
- [17] Sonderegger B, Holzer I, Kozeschnik E, et al. Particle distance distributions and their effect on precipitation strengthening. *Comput Mater Sci.* 2011;11:148–153.
- [18] Sommitsch C, Sonderegger B, Ahmadi M, et al. Microstructurally based modeling of creep

- deformation and damage in martensitic steels. In: Ravindran Mahesh editors Microstructurally based modeling of creep deformation and damage in martensitic steels. *Failure Analysis, IntechOpen* 2022; London, UK:10.5772/intechopen.104381
- [19] Orowan E. Problems of plastic gliding. *Proc Phys Soc.* 1940;52(1):8–22. doi: 10.1088/0959-5309/52/1/303
- [20] Basirat M, Shrestha T, Potirniche G, et al. A study of the creep behavior of modified 9Cr-1Mo steel using continuum-damage modeling. *Int J Plasticity.* 2012;37:95–107. doi: 10.1016/j.ijplas.2012.04.004
- [21] Dyson B, McLean M. Creep deformation of Engineering alloys: developments from physical modelling. *ISIJ Int.* 1990;30(10):802–911. doi: 10.2355/isiinternational.30.802
- [22] Owen D, Langdon T. Low stress creep behavior: an examination of Nabarro—herring and Harper—Dorn creep. *Mater Sci Eng.* 1996;A216(1–2):20–29. doi: 10.1016/0921-5093(96)10382-8
- [23] Wang Z, Muransky O, Zhu H, et al. On the kinetics of gamma prime (γ') precipitation and its strengthening mechanism in alloy 617 during a long-term thermal aging. *Materialia.* 2020;11:100682. doi: 10.1016/j.mtla.2020.100682
- [24] Tippelt B. Influence of temperature on microstructural parameters of cyclically deformed nickel single crystals. *Phil Mag Lett.* 1996;74(3):161–166. doi: 10.1080/095008396180317
- [25] Campbell C, Rukhin A. Evaluation of self-diffusion data using weighted means statistics. *Acta Mater.* 2011;59(13):5194–5201. doi: 10.1016/j.actamat.2011.04.055
- [26] Caillard D, Martin J. Chapter 8- dislocation climb. In: D. Caillard, J.L. Martin editors. Thermally activated mechanisms in crystal plasticity. Oxford, UK: Elsevier Science; 2003. pp. 281–319. doi:10.1016/S1470-1804(03)80038-X.
- [27] Hirth J, Lothe J. Theory of dislocations. 2nd ed. New York: John Wiley & Sons; 1982. pp. 569–573.
- [28] Lothe J. Theory of dislocation climb in Metals. *J Appl Phys.* 1960;31(6):1077–1081. doi: 10.1063/1.1735749
- [29] Special Metals datasheet no. SMC-29 on Inconel 617, 2005; available online: <https://www.specialmetals.com/documents/technical-bulletins/inconel/inconel-alloy-617.pdf>. (accessed 09-11-2023 from Linz, Austria).
- [30] CODATA, “The NIST reference on constants, units, and uncertainty,” 2014. [Online]. Available: <https://physics.nist.gov/cgi-bin/cuu/Value?k>. [Accessed 20 1 2023].
- [31] Haseeb A. Modeling of the effects of athermal flow strength and activation energy for dislocation glide on the nanoindentation creep of nickel thin film at room temperature. *Comp Mater Sci.* 2006;37(3):278–283. doi: 10.1016/j.commatsci.2005.07.006
- [32] Wang YM, Hamza AV, Ma E. Activation volume and density of mobile dislocations in plastically deforming nanocrystalline Ni. *Appl Phys Lett.* 2005;86(24):241917. doi: 10.1063/1.1946899
- [33] Xiao Y, Gan B, Sologubenko A, et al. Size- and strain rate-dependence of nickel and Ni–Co micropillars with varying stacking fault energy. *Mater Sci Eng.* 2021;800:140266. doi: 10.1016/j.msea.2020.140266
- [34] Burton B, Reynolds G. In defense of diffusional creep. *Mater Sci Eng.* 1995;191(1–2):135–141. doi: 10.1016/0921-5093(94)09643-0
- [35] Stechauner G, Kozeschnik E. Assessment of substitutional self-diffusion along short-circuit paths in al, fe and Ni. *Calphad.* 2014;47:92–99. doi: 10.1016/j.calphad.2014.06.008
- [36] Bose S, Banerjee R, Genc A, et al. Size induced metal-insulator transition in nanostructured niobium thin films: intra-granular and inter-granular contributions. *J Phys.* 2006;18(19):4553–4566. <https://www.doi.org/10.1088/0953-8984/18/19/010>
- [37] Sonderegger B. Modifications of stereological correction methods for precipitate parameters using transmission microscopy. *Ultramicroscopy.* 2006;106(10):941–950. doi: 10.1016/j.ultramic.2006.04.004
- [38] Schröders S, Sandlöbes S, Berkels B, et al. “On the structure of defects in the Fe7Mo6 μ -phase. *Acta Mater.* 2019;167:257–266. doi: 10.1016/j.actamat.2019.01.045
- [39] Riedlsperger F, Gsellmann B, Povoden-Karadeniz E, et al. Thermodynamic modelling and Microstructural study of Z-Phase formation in a ta-alloyed martensitic steel. *Material. Materials.* 2021;14(6):1332.
- [40] Lifshitz I, Slyozov V. The kinetics of precipitation from supersaturated solid solutions. *J Phys Chem Solids.* 1961;19(1–2):35–50. doi: 10.1016/0022-3697(61)90054-3
- [41] Wert C, Zener C. Interference of growing spherical precipitate particles. *J Appl Phys.* 1950;21(1):5–8. doi: 10.1063/1.1699422
- [42] Bullough C, Krein R, Lombardi P, et al, “Development of an ECCC interim creep rupture datasheet for alloy 617B using a strength averaging and blending approach”.*Proc. of 4th International ECCC Conference 2017*, pp. 1–11, Düsseldorf, Germany.
- [43] Schmidt K, “Komponentenverhalten im 700 °C-Kraftwerk- Numerische und experimentelle Untersuchungen”.*PhD Thesis at MPASTuttgart, Germany, 2013; 10.18419/opus-6436.*
- [44] Williams D, Carter C. Strain Fields. In: Transmission electron microscopy,” *A textbook for materials science.* Boston: Springer; 1996. pp. 412–419. doi: 10.1007/978-1-4757-2519-3_25
- [45] Riedlsperger F, Zuderstorfer G, Krenmayr B, et al. Application of a physically-based dislocation creep model to P92 for constructing TTR diagrams. *Mater High Temp.* 2022;39(2):161–166.
- [46] Zuderstorfer G, Riedlsperger F, Sonderegger B. CreeSo – software for creep simulation of complex alloys. *Mater High Temp.* 2022;39(6):596–602. doi: 10.1080/09603409.2022.2058237